Inorganic Chemistry

Communication

Cite This: Inorg. Chem. 2018, 57, 3679−3682

pubs.acs.org/IC

Beyond Crystal Engineering: Significant Enhancement of C_2H_2/CO_2 Separation by Constructing Composite Material

Hui Qiong Wu,[†] Chang Sheng Yan,[†] Feng Luo,*[,†,§] and Rajamani Krishna*[,‡]

[†]School of Biology, Chemistry and Material Science, East China University of Technology, NanChang, Jiangxi 344000, China
[‡]Van't Hoff Institute for Molecular Sciences, University of Amsterdam, Science Park 904, 1098 XH Amsterdam, The Netherlands
[§]College of Chemistry and Chemical Engineering, Hunan University of Science and Technology, XiangTan, HuNan 411201, China

Supporting Information

ABSTRACT: Different from the established crystal engineering method for enhancing gas-separation performance, we demonstrate herein a distinct approach. In contrast to the pristine MOF (metal−organic framework) material, the C_2H_2/CO_2 separation ability for the resultant Ag NPs (nanoparticle)@Fe_2O_3@MOF composite material, estimated from breakthrough calculations, is greatly enhanced by 2 times, and further magnified up to 3 times under visible light irradiation.

The rich potential of metal−organic frameworks (MOFs) for separating a wide variety of gaseous mixtures is the subject of intensive research in the published literature.[1−4] In particular, some difficult separations such as C_2H_2/CO_2 and C_2H_2/C_2H_4 mixtures, mainly due to their comparable size and physical nature, are highly interesting but remain a challenging task.[5−10] To this end, several approaches based on crystal engineering techniques relying on precise molecule design have been attested to show outstanding separation performance;[5−10] however, there is still no report by using simple physical or chemical methods, especially using light,[11,12] to enhance gas separation, which inherently is expected to enable general applicability beyond crystal engineering techniques.

To seek a possible solution, we draw a protocol, as shown in Scheme 1. The considerations are listed as follows. (i) Ag NPs can give a selective reaction with C_2H_2 to generate π-complexation formation[13] and thus afford preferable adsorption to C_2H_2. (ii) The Ag NP is one of the best NPs to render a plasmon-driven photothermal effect.[14] To meet the industrial demand of large-scale production, we herein launched a modified coprecipitation method to prepare Ag NPs@MOF composites in a rapid and in situ manner. After carrying out C_2H_2 and CO_2 adsorption studies, we found that the C_2H_2/CO_2 separation ability in the resultant Ag NPs@Fe_2O_3@MOF materials is significantly enhanced, relative to the pristine MOF material.

In the literature, the coprecipitation method has been developed to prepare oxide-supported noble-metal catalysts such as Ag, Au, Pd, or Pt@Fe_2O_3 composites, due to its convenience, low cost, and high-yield fabrication.[15] However, we also note some limits for such methods such as additional high-temperature treatment above 400 °C that is beyond the heat endurance for most MOFs and reduction by hot hydrogen that would add potential danger. Very recently, we launched a surface-enriching method to give an in situ and rapid preparation of the Fe_2O_3@MOF composite, due to a unique surface reaction between Fe^{3+} and the MOF substrate.[16,17] Further, the lower potential of Fe^{2+} (0.771 V), relative to Ag^+ (0.799 V), agrees with the thermodynamic reduction of Ag^+-to-Ag^0 by Fe^{2+} ions. Taking the above discussions into account, we propose here a modified coprecipitation method to prepare Ag NPs@ Fe_2O_3@MOF composites (Scheme 1).

Scheme 1. A Draft of Modified Coprecipitation Method for Preparation of Ag NPs@Fe_2O_3@MOF Composite and Schematic Illustration of Photoinduced Enhancement of C_2H_2/CO_2 Separation, Where Due to a Preferential Adsorption of C_2H_2 over CO_2 from Ag NPs the Released Amount of Guest Molecule Caused by Plasmon-Driven Photothermal Effect under Visible Light Irradiation Is Different for C_2H_2 and CO_2 Molecules

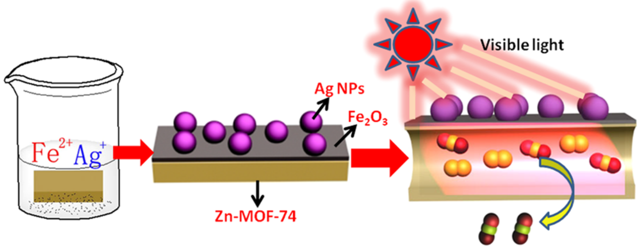

The materials were synthesized by stirring the solution of $AgNO_3$ and $FeSO_4$ in a ratio of 1:1 with the addition of 150 mg of Zn-MOF-74 within 1 min. Dependent on the different concentrations of $AgNO_3$ (100, 500, and 1000 ppm) in this reaction system, composites with a loading of 0.1 wt % Ag@2.2 wt % Fe_2O_3, 0.31 wt % Ag@3.3 wt % Fe_2O_3, and 0.44 wt % Ag@ 4.4 wt % Fe_2O_3 were obtained and are respectively named Ag@Fe_2O_3@Zn-MOF-74-I (*ab.* **I**), Ag@Fe_2O_3@Zn-MOF-74-II (*ab.* **II**), and Ag@Fe_2O_3@Zn-MOF-74-III (*ab.* **III**). The Ag NPs and Fe_2O_3 contents are determined by ICP-OES (inductively coupled plasma optical emission spectrometry).

Morphologies of the resulted samples were characterized by both scanning electron microscopy (SEM, Figure S1a, b, and c) and transmission electron microscopy (TEM, Figure S 1d, e, and f). It is clear that Ag NPs and Fe_2O_3 are successfully loaded on the surface of Zn-MOF-74, and the content of Ag NPs and Fe_2O_3 increases along with the increasing concentration of $AgNO_3$. The

Received: February 6, 2018
Published: March 21, 2018

ACS Publications © 2018 American Chemical Society

DOI: 10.1021/acs.inorgchem.8b00341
Inorg. Chem. 2018, 57, 3679−3682

TEM images show near-spherical Ag NPs with a size of ~20 nm. A close examination using high-resolution TEM (HRTEM, Figure S1g, h, and i) confirms a crystalline character with a lattice spacing of 0.25 nm, comparable with the typical lattice fringe of Ag NPs (d_{111}).[18] Note that, as shown in Figure S1i, a multilevel structure with an obvious outline is observed in the resulted Ag@ Fe_2O_3 @Zn-MOF-74-III samples, suggesting the coprecipitation of Ag NPs with Fe_2O_3, rather than direct enrichment of Ag NPs on the MOF substrate during the generation of such products.

The loading of Ag NPs and Fe_2O_3 is further confirmed by XPS (X-ray photoelectron spectroscopy) and powder X-ray diffraction (PXRD). The spectra of Ag 3d show the $3d_{3/2}$ and $3d_{5/2}$ signals at 374.5 and 368.5 eV (Figure S2), respectively, belonging to a typical character of metallic (zerovalent) silver,[18] while the XPS spectra of Fe 2p displays four peaks, Fe $2p_{2/3}$, Fe $2p_{1/2}$, and their satellites, centering at 711.5, 718.7, 725.2, and 733.8 eV (Figure S3), respectively, in accordance with the electronic state of α-Fe_2O_3.[16,17] In the PXRD patterns (Figure 1a), not only Bragg peaks observed in the resulted samples match well with the simulated data of Zn-MOF-74, suggesting good maintenance of the MOF substrate, but also some detectable signs characterized to be Ag NPs such as (200), (220), and (311)[18] and α-Fe_2O_3 such as (012) and (300) are observed.[16,17] Their porosities are investigated by N_2 adsorption at 77 K, and the results are shown in Figure 1b, giving a microporous type I curve. BET surface areas are 597, 689, and 936 cm^2/g, respectively, comparable with the reported value (747 cm^2/g)[19] for Zn-MOF-74. The pore size distributions of these materials are also analyzed, comparable with the reported value in Zn-MOF-74.[19] Furthermore, their light absorbencies are tested by UV−vis spectra (Figure S4). In contrast to the pristine Zn-MOF-74, the samples with increasing Ag content afford significantly increased absorbability at 400−800 nm, due to a characteristic contribution from Ag NPs.[14]

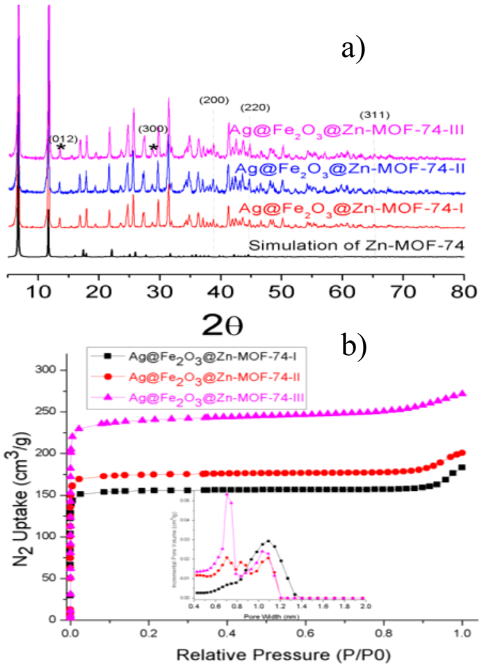

Figure 1. (a) Simulated PXRD patterns of Zn-MOF-74 and experimental PXRD patterns of samples **I**, **II**, and **III**. The highlight by "*" and dashed present characteristic Bragg peaks of α-Fe_2O_3 and Ag NPs, respectively. (b) N_2 adsorption isotherms of samples **I**, **II**, and **III** at 77 K. The insert is their pore size distribution.

To confirm our concept, we carried out systemic gas-adsorption studies on these resultant composites. The C_2H_2 and CO_2 adsorption in the dark at 293 K is measured and shown in Figure S5. The C_2H_2 uptake capacity at 100 kPa is 135, 146, and 150 cm^3/g for materials **I**, **II**, and **III**, respectively. In comparison to the pristine Zn-MOF-74 giving 124 cm^3/g,[20] it is clear that increasing the Ag content benefits the enhancement of C_2H_2 uptake with the biggest increase up to 21%. As expected, the opposite trend is observed for CO_2 uptake, and materials **I**, **II**, and **III** only afford 100, 117, and 115 cm^3/g of CO_2 uptake at 100 kPa, respectively, less than corresponding value of 120 cm^3/g for Zn-MOF-74.[20] Accordingly, the difference between C_2H_2 and CO_2 adsorption, as shown in Figure S5, is 35, 29, and 35 cm^3/g, respectively. Notably, the value (35 cm^3/g) is almost 9 times bigger than that observed for pristine Zn-MOF-74 (just 4 cm^3/g), indicative of large enhancement of C_2H_2 selectivity over CO_2 via Ag loading. Most importantly, although a decrease in both C_2H_2 and CO_2 adsorption capacity is observed for these Ag-loaded materials due to the plasmon-driven photothermal effect under visible light irradiation, however, some discrepancy for such a decrease is also observed. And thereby the difference in C_2H_2 and CO_2 adsorption is increased to be 37, 35, and 39 cm^3/g, respectively, strongly suggesting that such a plasmon-driven photothermal effect enables distinct release for various guest molecules and further enhances adsorption selectivity.

To confirm the above claim, the C_2H_2/CO_2 selectivity for the materials **I**, **II**, and **III** in the dark and Vis is estimated by ideal adsorbed solution theory (IAST) calculations.[20] In contrast to the selectivity (S_{ads} = 2.61) of Zn-MOF-74 at 100 kPa and room temperature, the selectivity for the Ag-loaded materials is improved to be 2.88, 3.21, and 3.33 in the dark and further increased up to 4.35, 4.37, and 4.73 under Vis irradiation, respectively (Figure 2a and b). In this regard, materials **III** under Vis irradiation afford the highest adsorption selectivity, almost 2 times bigger than that for Zn-MOF-74. Such selectivity is also compared with UTSA-74,[20] one of the best established candidates for C_2H_2/CO_2 separation. We note that the selectivity of Ag@Fe_2O_3@Zn-MOF-74-III under Vis is lower than that of UTSA-74. However, as stressed in the literature,[21] C_2H_2/CO_2 separations in fixed bed adsorbers are also dictated by C_2H_2 uptake capacities. Figure 2c and d present the IAST calculations of the C_2H_2 uptake capacity for a 50:50 C_2H_2/CO_2 mixture at 293 K for materials **I**, **II**, and **III** in the dark and in the Vis, Zn-MOF-74, and USTA-74, respectively. Generally speaking, the C_2H_2 uptake capacity increases with increasing content of Ag. The highest C_2H_2 uptake capacity is achieved with materials **III** under a Vis trigger; its uptake capacity is compared in Figure 2d with UTSA-74 and Zn-MOF-74, significantly higher, by 2 times, than that of UTSA-74 and Zn-MOF-74.

The performance of industrial fixed bed adsorbers is dictated by a combination of adsorption selectivity and uptake capacity.[21] To properly weigh the selectivity and capacity metrics for evaluation of materials **I**, **II**, and **III** in the application of C_2H_2/CO_2 separation, we performed transient breakthrough simulations using the simulation methodology described in the literature.[20] Figure 2e presents the transient breakthrough simulations for separation of an equimolar C_2H_2/CO_2 mixture with partial pressures of 50 kPa by materials **III** under Vis. During the initial transience, the effluent gas contains pure CO_2, and this continues until C_2H_2 starts breaking through because its uptake capacity has been reached.

Longer breakthrough times of C_2H_2 are desirable because it reduces the frequency of regenerations. Regeneration costs are

DOI: 10.1021/acs.inorgchem.8b00341
Inorg. Chem. 2018, 57, 3679−3682

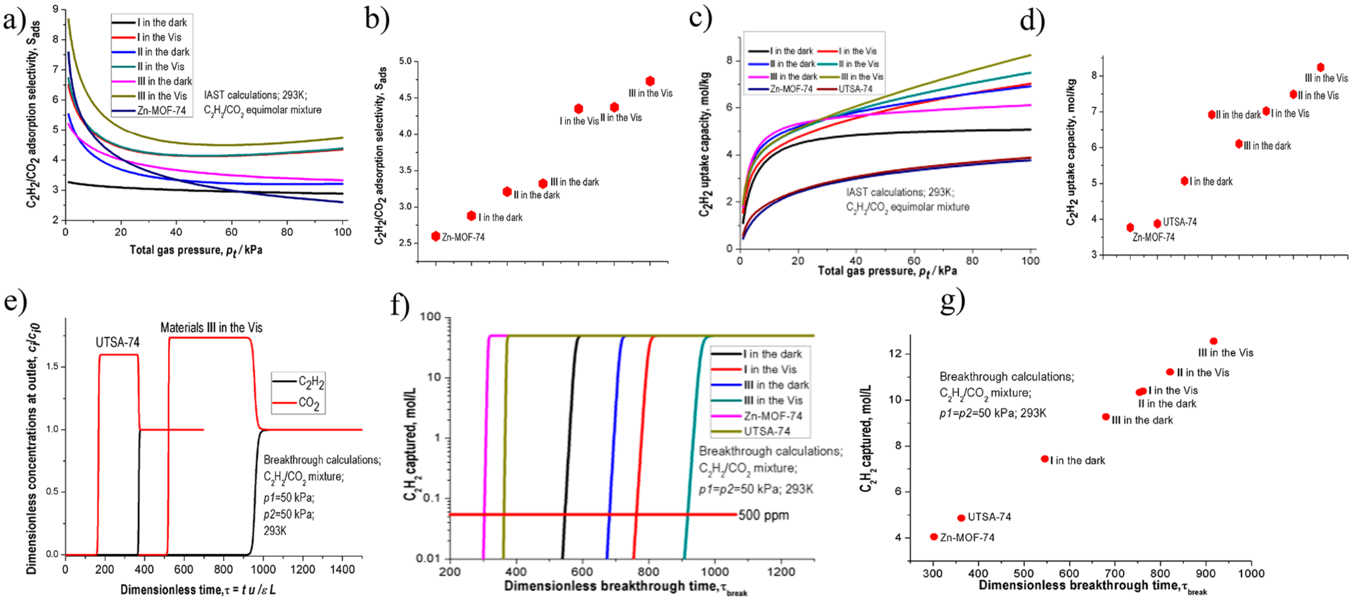

Figure 2. (a) IAST calculations of the adsorption selectivity, S_{ads}, for separation of 50/50 C_2H_2/CO_2 mixture at 293 K for materials **I**, **II**, and **III** in the dark and Vis, and Zn-MOF-74, respectively. (b) A comparison of S_{ads} for these materials at 293 K and 100 kPa. (c) IAST calculations of the C_2H_2 uptake capacity for 50/50 C_2H_2/CO_2 mixture at 293 K for materials **I**, **II**, and **III** in the dark and Vis, USTA-74, and Zn-MOF-74, respectively. (d) A comparison of IAST calculations of the C_2H_2 uptake capacity for these materials at 293 K and 100 kPa. (e) Transient breakthrough simulations for separation of equimolar C_2H_2/CO_2 mixture with partial pressures of 50 kPa each using materials **III** in the Vis and UTSA-74. (f) Comparison of % C_2H_2 in the exit gas from packed beds plotted as a function of the dimensionless time using materials **I** and **III** in the dark and Vis, Zn-MOF-74, and UTSA-74. (g) Comparison of the moles of C_2H_2 captured per liter of material during the interval for which the product gas is 99.95% CO_2, plotted as a function of the dimensionless breakthrough time, τ_{break}.

the major contributors to energy use in fixed bed operations. We note that the breakthrough of C_2H_2 for UTSA-74 occurs at a dimensionless time that is half the value of that for materials **III** under Vis. The reason, as evidenced from Figure 2c, is that the C_2H_2 uptake capacity of materials **III** under Vis is about 1 times higher than that of UTSA-74.

A comparison of % C_2H_2 in the exit gas for beds packed with materials **I**, **II**, and **III** in the dark and Vis, plotted as a function of the dimensionless time, is also calculated, where the breakthrough times are longer with increasing Ag content, because the C_2H_2 uptake capacity increases with increasing content of Ag (Figure 2f). Moreover, a similar comparison among materials **I**, **II**, and **III** in the dark and Vis, UTSA-74, and Zn-MOF-74 is presented as Figure 2f and g. Notably, even in the dark, the breakthrough times with materials **I** are significantly higher than with UTSA-74, and Zn-MOF-74. As described in the literature,[20] the impurity level of acetylene in the gas mixture exiting the fixed-bed packed with materials **I**, **II**, and **III** in the dark and Vis, UTSA-74, and Zn-MOF-74 is calculated. We define the breakthrough time, τ_{break}, as the time at which the exit gas contains <0.05% = 500 ppm of C_2H_2. The amount of C_2H_2 captured during the time interval 0−τ_{break} can be determined from a material balance and is expressed as moles of C_2H_2 captured per liter of framework material against τ_{break}. Accordingly, the values of τ_{break} have the following hierarchy, Zn-MOF-74[15] < UTSA-74[15] < materials **I** in the dark < ... < materials **III** in the Vis, strongly suggesting superior application in C_2H_2/CO_2 separation for these Ag-loaded materials, especially these in the Vis trigger. Note that our performance also exceeds other reported porous materials such as HOF-3,[22] ZJU-60a,[23] PCP-33,[24] and [Mn(bdc)(dpe)].[25]

In conclusion, we have shown a highly effective and facile method beyond crystal engineering to enhance the gas-separation ability of MOF. The results show that loading Ag on Zn-MOF-74 helps to increase C_2H_2 adsorption capacity, leading to enhanced C_2H_2/CO_2 adsorption selectivity and separation performance. Meanwhile, the plasmon-driven photothermal effect under visible light irradiation further enhances C_2H_2/CO_2 adsorption selectivity and separation performance, demonstrating a potentially low energy strategy by using visible light as a driving force for modulating gas separation.

■ ASSOCIATED CONTENT

Ⓢ Supporting Information

The Supporting Information is available free of charge on the ACS Publications website at DOI: 10.1021/acs.inorgchem.8b00341.

Material involved in synthesis and additional figures (PDF)

■ AUTHOR INFORMATION

Corresponding Authors

*E-mail: ecitluofeng@163.com.
*E-mail: R.Krishna@contact.uva.nl.

ORCID

Feng Luo: 0000-0001-6380-2754
Rajamani Krishna: 0000-0002-4784-8530

Notes

The authors declare no competing financial interest.

■ ACKNOWLEDGMENTS

This work was supported by the NSF of China (21661001 and 21661002), the Innovation Fund Designated for Graduate Students of Jiangxi Province (YC2017-S275).

REFERENCES

(1) Furukawa, H.; Cordova, K. E.; O'Keeffe, M.; Yaghi, O. M. The chemistry and applications of metal-organic frameworks. *Science* **2013**, *341*, 1230444.

(2) Adil, K.; Belmabkhout, Y.; Pillai, R. S.; Cadiau, A.; Bhatt, P. M.; Assen, A. H.; Maurin, G.; Eddaoudi, M. Gas/vapour separation using ultra-microporous metal-organic frameworks: insights into the structure/separation relationship. *Chem. Soc. Rev.* **2017**, *46*, 3402−3430.

(3) Li, B.; Wen, H. M.; Cui, Y. J.; Zhou, W.; Qian, G. D.; Chen, B. L. Emerging multifunctional metal-Organic framework materials. *Adv. Mater.* **2016**, *28*, 8819−8860.

(4) Cui, Y. J.; Li, B.; He, H. J.; Zhou, W.; Chen, B. L.; Qian, G. D. Metal-organic frameworks as platforms for functional materials. *Acc. Chem. Res.* **2016**, *49*, 483−493.

(5) Cadiau, A.; Adil, K.; Bhatt, P. M.; Belmabkhout, Y.; Eddaoudi, M. A metal-organic framework-based splitter for separating propylene from propane. *Science* **2016**, *353*, 137−140.

(6) Liao, P. Q.; Huang, N. Y.; Zhang, W. X.; Zhang, J. P.; Chen, X. M. Controlling guest conformation for efficient purification of butadiene. *Science* **2017**, *356*, 1193−1196.

(7) Cui, X. L.; Chen, K. J.; Xing, H. B.; Yang, Q. W.; Krishna, R.; Bao, Z. B.; Wu, H.; Zhou, W.; Dong, X. L.; Han, Y.; Li, B.; Ren, Q. L.; Zaworotko, M. J.; Chen, B. L. Pore chemistry and size control in hybrid porous materials for acetylene capture from ethylene. *Science* **2016**, *353*, 141−144.

(8) Matsuda, R.; Kitaura, R.; Kitagawa, S.; Kubota, Y.; Belosludov, R. V.; Kobayashi, T. C.; Sakamoto, H.; Chiba, T.; Takata, M.; Kawazoe, Y.; Mita, Y. Highly controlled acetylene accommodation in a metal-organic microporous material. *Nature* **2005**, *436*, 238−241.

(9) Chen, K. J.; Scott, H. S.; Madden, D. G.; Pham, T.; Kumar, A.; Bajpai, A.; Lusi, M.; Forrest, K. A.; Space, B.; Perry, J. J.; Zaworotko, M. J. Benchmark C_2H_2/CO_2 and CO_2/C_2H_2 separation by two closely related hybrid ultramicroporous materials. *Chem.* **2016**, *1*, 753−765.

(10) Lin, R. B.; Li, L. B.; Wu, H.; Arman, H.; Li, B.; Lin, R. G.; Zhou, W.; Chen, B. L. Optimized separation of acetylene from carbon dioxide and ethylene in a microporous material. *J. Am. Chem. Soc.* **2017**, *139*, 8022−8028.

(11) Li, H. Q.; Hill, M. R. Low-energy CO_2 release from metal-organic frameworks triggered by external stimuli. *Acc. Chem. Res.* **2017**, *50*, 778−786.

(12) Fan, C. B.; Le Gong, L.; Huang, L.; Luo, F.; Krishna, R.; Yi, X. F.; Zheng, A. M.; Zhang, L.; Pu, S. Z.; Feng, X. F.; Luo, M. B.; Guo, G. C. Significant enhancement of C_2H_2/C_2H_4 separation by a photochromic diarylethene unit: a temperature- and light-responsive separation switch. *Angew. Chem., Int. Ed.* **2017**, *56*, 7900−7906.

(13) Yang, R. T. *Adsorbents: Fundamentals and Applications*; Wiley-Interscience: Hoboken, NJ, 2003.

(14) Li, H. Q.; Hill, M. R.; Doblin, C.; Lim, S.; Hill, A. J.; Falcaro, P. Visible light triggered CO_2 liberation from silver nanocrystals incorporated metal-organic frameworks. *Adv. Funct. Mater.* **2016**, *26*, 4815−4821.

(15) Qiao, B. T.; Wang, A. Q.; Yang, X. F.; Allard, L. F.; Jiang, Z.; Cui, Y. T.; Liu, J. Y.; Li, J.; Zhang, T. Single-atom catalysis of CO oxidation using Pt_1/FeO_x. *Nat. Chem.* **2011**, *3*, 634−641.

(16) Yan, C. S.; Gao, H. Y.; Le Gong, L.; Ma, L. F.; Dang, L. L.; Zhang, L.; Meng, P. P.; Luo, F. MOF surface method for the ultrafast and one-step generation of metal-oxide-NP@MOF composites as lithium storage materials. *J. Mater. Chem. A* **2016**, *4*, 13603−13610.

(17) Xiong, Y. Y.; Li, J. Q.; Yan, C. S.; Gao, H. Y.; Zhou, J. P.; Gong, L. L.; Luo, M. B.; Zhang, L.; Meng, P. P.; Luo, F. MOF catalysis of Fe^{II}-to-Fe^{III} reaction for an ultrafast and one-step generation of the Fe_2O_3@MOF composite and uranium(VI) reduction by iron(II) under ambient conditions. *Chem. Commun.* **2016**, *52*, 9538−9541.

(18) Luc, W.; Collins, C.; Wang, S. W.; Xin, H. L.; He, K.; Kang, Y. J.; Jiao, F. Ag-Sn bimetallic catalyst with a core-shell structure for CO_2 reduction. *J. Am. Chem. Soc.* **2017**, *139*, 1885−1893.

(19) Zhang, Z. J.; Xiang, S. C.; Chen, B. L. Microporous metal-organic frameworks for acetylene storage and separation. *CrystEngComm* **2011**, *13*, 5983−5992.

(20) Luo, F.; Yan, C. S.; Dang, L. L.; Krishna, R.; Zhou, W.; Wu, H.; Dong, X. L.; Han, Y.; Hu, T. L.; O'Keeffe, M.; Wang, L. L.; Luo, M. B.; Lin, R. B.; Chen, B. L. UTSA-74: a MOF-74 isomer with two accessible binding sites per metal center for highly selective gas separation. *J. Am. Chem. Soc.* **2016**, *138*, 5678−5684.

(21) Bao, Z. B.; Chang, G. G.; Xing, H. B.; Krishna, R.; Ren, Q. L.; Chen, B. L. Potential of microporous metal-organic frameworks for separation of hydrocarbon mixtures. *Energy Environ. Sci.* **2016**, *9*, 3612−3641.

(22) Li, P.; He, Y.; Zhao, Y.; Weng, L.; Wang, H.; Krishna, R.; Wu, H.; Zhou, W.; O'Keeffe, M.; Han, Y.; Chen, B. A rod-packing microporous hydrogen-bonded organic framework for highly selective separation of C_2H_2/CO_2 at room temperature. *Angew. Chem., Int. Ed.* **2015**, *54*, 574−577.

(23) Duan, X.; He, Y. B.; Zhang, Q.; Wu, C.; Cai, J. F.; Cui, Y. J.; Yang, Y.; Qian, G. D.; Chen, B. L.; Krishna, R. A new metal−organic framework with potential for adsorptive separation of methane from carbon dioxide, acetylene, ethylene, and ethane established by simulated breakthrough experiments. *J. Mater. Chem. A* **2014**, *2*, 2628−2633.

(24) Duan, J. G.; Jin, W. Q.; Krishna, R. Natural gas purification using a porous coordination polymer with water and chemical stability. *Inorg. Chem.* **2015**, *54*, 4279−4284.

(25) Foo, M. L.; Matsuda, R.; Hijikata, Y.; Krishna, R.; Sato, H.; Horike, S.; Hori, A.; Duan, J. G.; Sato, Y.; Kubota, Y.; Takata, M.; Kitagawa, S. An adsorbate discriminatory gate effect in a flexible porous coordination polymer for selective adsorption of CO_2 over C_2H_2. *J. Am. Chem. Soc.* **2016**, *138*, 3022−3030.

Supporting information

Beyond Crystal Engineering: Significant Enhancement of C_2H_2/ CO_2 Separation by Constructing Composite Material

Hui Qiong Wu,[a] Chang Sheng Yan,[a] Feng Luo,[ac]* and Rajamani Krishna[b]*

[a]School of Biology, Chemistry and Material Science, East China University of Technology , NanChang, Jiangxi 344000, China, E-mail: ecitluofeng@163.com

[b]Van 't Hoff Institute for Molecular Sciences, University of Amsterdam, Science Park 904, 1098 XH Amsterdam, The Netherlands, E-mail: R.Krishna@contact.uva.nl

[c]College of Chemistry and Chemical Engineering, Hunan University of Science and Technology, XiangTan, HuNan, 411201, China

Experimental detail.

Synthesis of Zn-MOF-74. A mixture of $Zn(NO_3)_2\cdot 6H_2O$ (0.0604 g, 0.203 mmol), 2,5-dihydroxy terephthalic acid (0.0191 g, 0.096 mmol), N,N-dimethylformamide (DMF) (2ml), isopropyl alcohol (0.1 mL) and H_2O (2 mL) was placed in a closed 25 ml Teflon reactor and heated at 105°C for 1200 min, in turn cooled to room temperature, produced brown needle-shaped crystals were got and dried in 71 % yield (based on Zn) at room temperature.

Synthesis of materials I, II and III. 150 mg Zn-MOF-74 samples were added into a solution (H_2O, 10 mL) containing 1 mL $FeSO_4$ (100 ppm, 500 ppm, and 1000 ppm, respectively) and 1 mL $AgNO_3$ (100 ppm, 500 ppm, and 1000 ppm, respectively) to stir for one minute at room temperature and ambience, then the resulted solid samples were separated by centrifugal separation, and washed three times by distilled water, next dried naturally.

Materials and general methods.

All the reagents used in this work are purchased from Alfa without any purification. X-ray powder diffraction were collected by a Bruker AXSD8 Discover powder diffractometer at 40 kV, 40 mA for Cu Kα, ($\lambda = 1.5406$Å). The simulated powder patterns were calculated by Mercury 1.4. The purity of the bulk products were determined by comparison of the simulated and experimental PXRD patterns. SEM measurements were carried out using a Oxford X-max microscope. XPS experiments were performed in a Theta probe (Thermo Fisher) using monochromated Al Kα x-rays at *hv*=1486.6 eV.

The gas sorption isotherms were collected on a Belsorp-max. Ultrahigh-purity-grade (>99.999%) C_2H_2 and CO_2 gases were used in this adsorption measurement. To maintain the experimental temperatures liquid nitrogen (77 K), and water bath (293 K) were used respectively.

Before carrying out adsorption experiments, the as-synthesized samples (150 mg) were immerged in CH_3OH for three days, then degassed automatically in Belsorp-max at 60℃ for 24 h to generate the activated samples.

The adsorption data in the dark is obtained based on the samples enwraped by foil at the exterior, while the adsorption data in the Vis is obtained based on the samples with continuous Vis irradiation.

The Vis irradiation is carried out by Mejiro Genossen MVL-210 (3.5 W/cm^2) . The distance between the light source and samples is about 80 cm.

Fitting of pure component isotherms.

The pure component isotherm data for C_2H_2 measured at 293 K in these Ag@Fe_2O_3@Zn-MOF-74 materials, in the dark and Vis, were fitted with the dual-site Langmuir model

$$q = q_{A,sat}\frac{b_A p}{1+b_A p} + q_{B,sat}\frac{b_B p}{1+b_B p} \tag{1}$$

The pure component isotherm data for CO_2 measured at 293 K in these Ag@Fe_2O_3@Zn-MOF-74 materials, in the dark and Vis,, were fitted with the single-site Langmuir model

$$q = q_{sat}\frac{b_A p}{1+b_A p} \tag{2}$$

The fitted parameter values are presented in Table 1, and Table 2.

Table S1. Dual-site Langmuir parameter fits for C_2H_2 and single-site Langmuir parameter fits for CO_2 in these Ag@Fe_2O_3@Zn-MOF-74 materials in the dark.

$q = q_{A,sat}\frac{b_A p}{1+b_A p} + q_{B,sat}\frac{b_B p}{1+b_B p}$		Site A		Site B	
		$q_{A,sat}$ mol/kg	b_A Pa^{-1}	$q_{B,sat}$ mol/kg	b_B Pa^{-1}
Materials **I**	C_2H_2	7.0	3.93×10^{-4}		

Materials **II**	C_2H_2	10.0	7.38×10^{-6}	6.0	9.19×10^{-4}
Materials **III**	C_2H_2	6.9	7.37×10^{-4}	5.0	4.11×10^{-6}
Materials **I**	CO_2	7.4	1.13×10^{-4}		
Materials **II**	CO_2	9.2	1.02×10^{-4}		
Materials **III**	CO_2	8.8	1.07×10^{-4}		

Table S2. Dual-site Langmuir parameter fits for C_2H_2 and single-site Langmuir parameter fits for CO_2 in these Ag@Fe_2O_3@Zn-MOF-74 materials with Vis light.

$q = q_{A,sat}\frac{b_A p}{1+b_A p} + q_{B,sat}\frac{b_B p}{1+b_B p}$		Site A		Site B	
		$q_{\mathrm{A,sat}}$ mol/kg	b_{A} Pa^{-1}	$q_{\mathrm{B,sat}}$ mol/kg	b_{B} Pa^{-1}
Materials **I**	C_2H_2	10.3	1.07×10^{-5}	4.9	9.17×10^{-4}
Materials **II**	C_2H_2	12.0	9.36×10^{-6}	5.2	1.07×10^{-3}
Materials **III**	C_2H_2	30.0	3.63×10^{-6}	5.0	1.22×10^{-3}
Materials **I**	CO_2	8.0	8.19×10^{-5}		
Materials **II**	CO_2	8.4	9.21×10^{-5}		
Materials **III**	CO_2	9.0	7.09×10^{-5}		

IAST calculations of adsorption selectivities.

We consider the separation of binary C_2H_2/CO_2 mixtures. The adsorption selectivity for C_2H_2/CO_2 separation is defined by

$$S_{ads} = \frac{q_1/q_2}{p_1/p_2} \qquad (3)$$

q_1, and q_2 are the molar loadings in the adsorbed phase in equilibrium with the bulk gas phase with partial pressures p_1, and p_2.

Transient breakthrough simulations.

Transient breakthrough of C_2H_2/CO_2 mixtures in fixed bed adsorbers.

For the breakthrough simulations, the following parameter values were used: length of packed bed, $L = 0.3$ m; voidage of packed bed, $\varepsilon = 0.4$; superficial gas velocity at inlet, $u = 0.04$ m/s.

The total bulk gas phase is at setted temperature and 100 kPa. The partial pressures of C_2H_2, and CO_2 in the inlet feed gas mixture are, respectively, $p_1 = 50$ kPa, $p_2 = 50$ kPa. The transient breakthrough simulation results are presented in terms of a *dimensionless* time, τ, (x-axis), defined by dividing the actual time, t, by the characteristic time, $\frac{L\varepsilon}{u}$. The y-axis is the dimensionless concentrations at the outlet of the adsorber, normalized with respect to the inlet feed concentrations.

Table S3. Breakthrough calculations for separation of 50/50 C_2H_2/CO_2 mixture.

	Dimensionless breakthrough time τ_{break}	C_2H_2 adsorbed during 0 - τ_{break} (mol L^{-1})
Materials **I** in the Vis	762	10.39
Materials **II** in the Vis	821	11.22
Materials **III** in the Vis	917	12.56
Materials **I** in the dark	546	7.44
Materials **II** in the dark	754	10.33
Materials **III** in the dark	680	9.28
UTSA-74	362	4.86
Zn-MOF-74	303	4.06

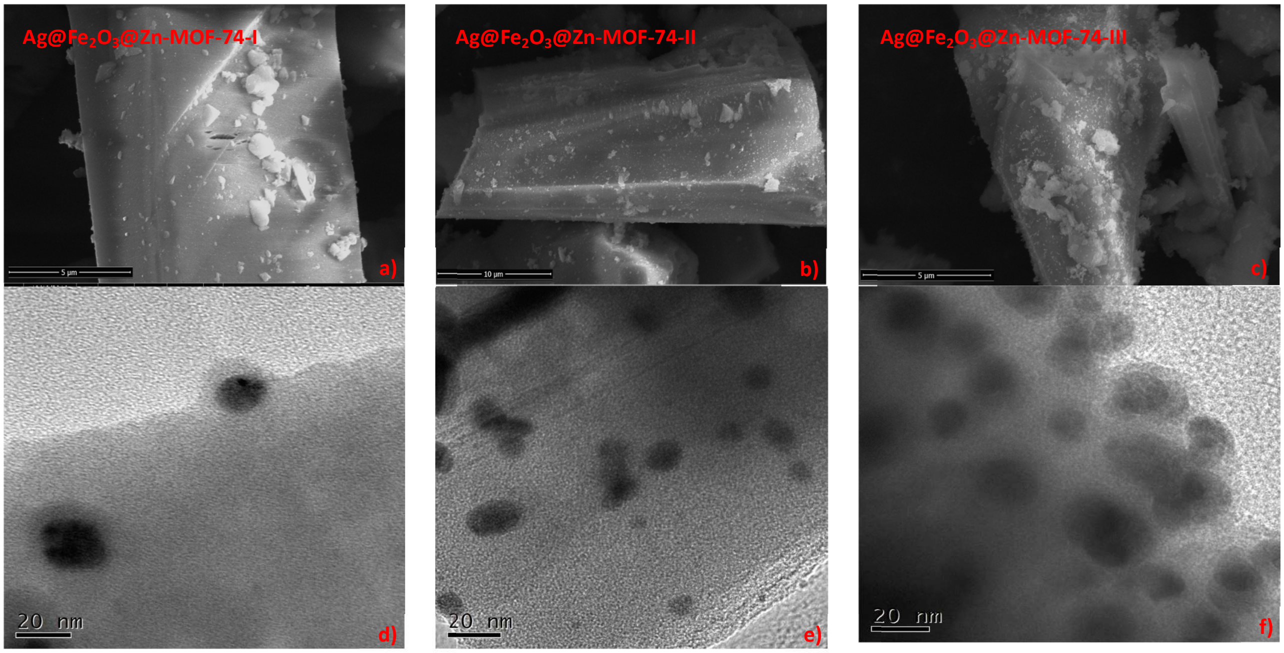

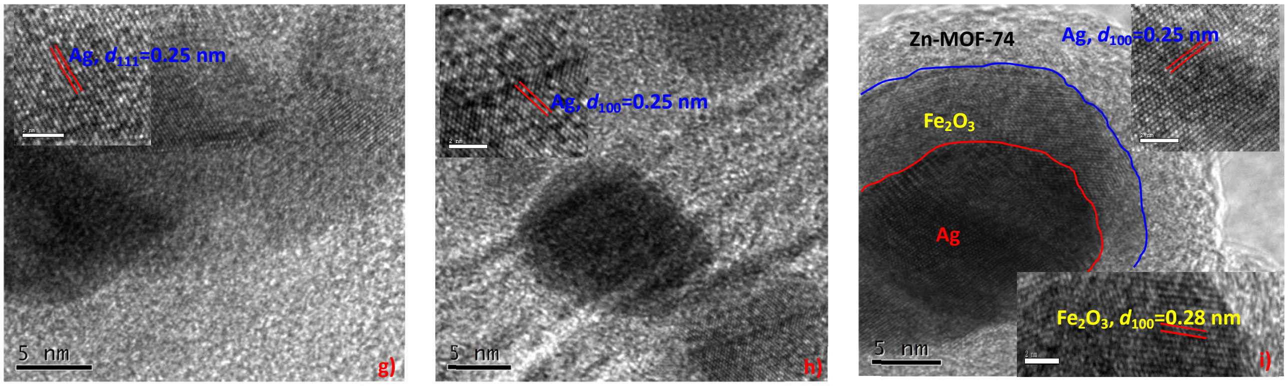

Figure S1. SEM images of a) samples I, b) samples II, and c) samples III. TEM images of d) samples I, e) samples II, and f) samples III. HRTEM images of g) samples I, h) samples II, and i) samples III. The inserts are corresponding FFT images.

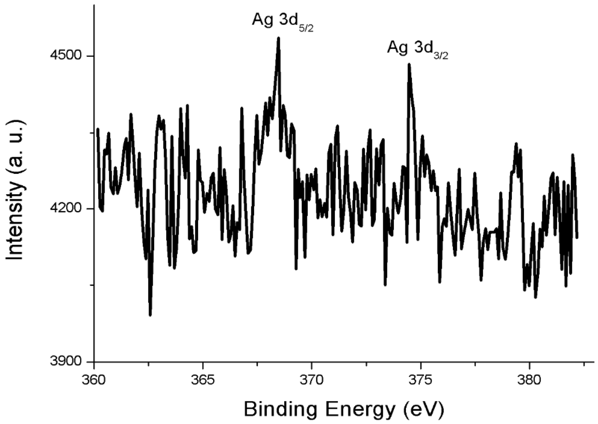

Figure S2. XPS spectroscopy of Ag@Fe$_2$O$_3$@Zn-MOF-74-**III**. Ag$_{3d}$ for Ag NPs in the present composite.

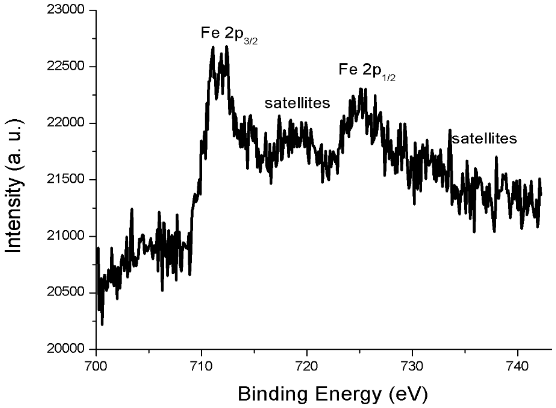

Figure S3. XPS spectroscopy of Ag@Fe$_2$O$_3$@Zn-MOF-74-**III**. Fe$_{2p}$ for Fe$_2$O$_3$ in the present composite.

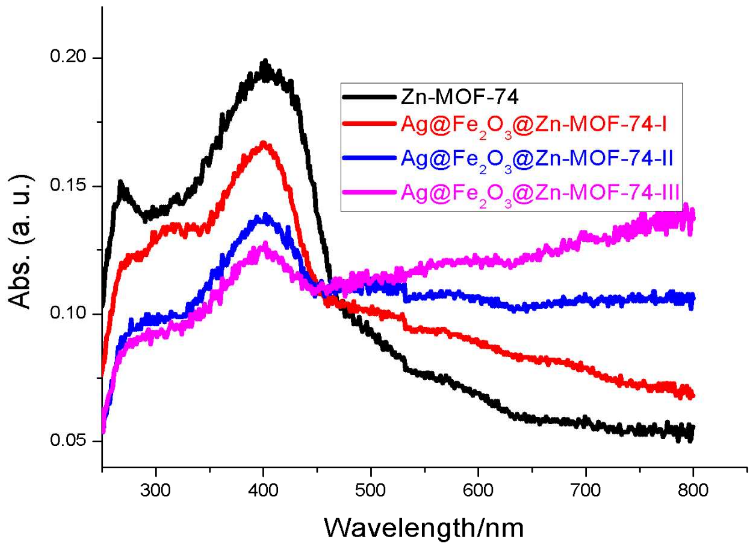

Figure S4. The UV-Vis spectra of Zn-MOF-74, and samples **I**, **II**, and **III** in the solid.

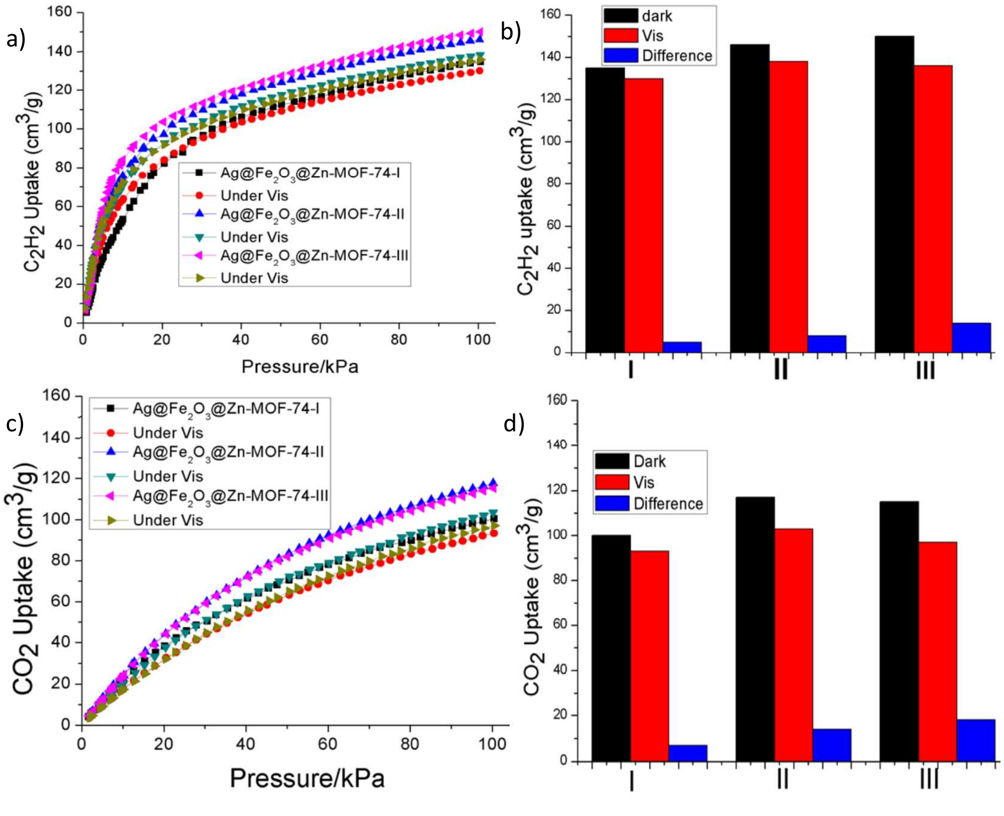

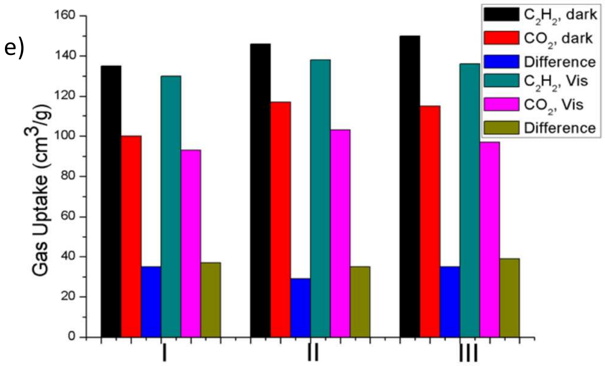

Figure S5. a) The C_2H_2 adsorption isotherms of materials **I**, **II**, and **III** in the dark and Vis; b) histogram of C_2H_2 uptake capacity at 293K and 100 kPa in the dark and Vis, as well as the difference between them; c) the CO_2 adsorption isotherms of materials **I**, **II**, and **III** in the dark and Vis; d) histogram of CO_2 uptake capacity at 293K and 100 kPa in the dark and Vis, as well as the difference between them; e) histogram of both C_2H_2 and CO_2 uptake capacity at 293K and 100 kPa in the dark and Vis, as well as the difference between them.